# Two-dimensional photonic crystals for engineering atom–light interactions

Su-Peng Yu[a,1], Juan A. Muniz[a,1], Chen-Lung Hung[b,c], and H. J. Kimble[a,2]

[a]Norman Bridge Laboratory of Physics, California Institute of Technology, Pasadena, CA 91125; [b]Department of Physics and Astronomy, Purdue University, West Lafayette, IN 47907; and [c]Purdue Quantum Center, Purdue University, West Lafayette, IN 47907

Contributed by H. J. Kimble, May 9, 2019 (sent for review December 31, 2018; reviewed by Antonio Badolato and Hannes Pichler)

**We present a 2D photonic crystal system for interacting with cold cesium (Cs) atoms. The band structures of the 2D photonic crystals are predicted to produce unconventional atom–light interaction behaviors, including anisotropic emission, suppressed spontaneous decay, and photon-mediated atom–atom interactions controlled by the position of the atomic array relative to the photonic crystal. An optical conveyor technique is presented for continuously loading atoms into the desired trapping positions with optimal coupling to the photonic crystal. The device configuration also enables application of optical tweezers for controlled placement of atoms. Devices can be fabricated reliably from a 200-nm silicon nitride device layer using a lithography-based process, producing predicted optical properties in transmission and reflection measurements. These 2D photonic crystal devices can be readily deployed to experiments for many-body physics with neutral atoms and engineering of exotic quantum matter.**

nanophotonics | quantum optics | quantum many-body

The introduction of nanophotonics to the field of quantum optics and atomic physics greatly broadens the capabilities of atom–photon systems (1). Interaction with photonic structures such as tapered optical fibers (2–5), microcavities (6–8), and photonic crystal (PhC) waveguides (9–13) enables engineering of atom optical properties by modifying the local density of state (LDOS) of the electromagnetic field that interacts with the atoms. Such engineering capabilities have been actively explored in various solid-state systems such as quantum dots (14–16), color centers (17, 18), and embedded rare-earth ions (19–21). Among the variety of quantum emitters available today, the identical-particle nature of neutral atoms provides particular advantages in forming quantum many-body systems. When excited near a photonic structure, an array of neutral atoms can all radiatively couple to the shared photonic modes, exhibiting collective superradiant (10, 22) and subradiant (22) decay phenomena. A coherent collective Lamb shift has also been observed in a PhC with trapped atoms off-resonantly coupled to the band edge of a photonic band gap (11). Such collective coupling to common photonic modes effectively introduces interactions between neutral atoms, making it possible to engineer long-range spin Hamiltonians (using trapped atoms as spins) with controllable range and strength of interactions (23, 24), with pairwise interaction tunability (25), and even with atomic spin and motion coupling for creating novel crystalline phases (26). Furthermore, quantum emitters coupled to 1D waveguides have been proposed as a way to implement a basic universal quantum computer (27, 28).

Parallel to existing experimental studies of atom–photon coupling in quasi-linear waveguides and cavities, there has been substantial interest in engineering atom–light interactions in 2D photonic structures. One expects new phenomena to arise from the rich band structures and photonic transport properties in 2D geometries, such as anisotropic or directional atomic emission in a 2D PhC (29, 30), frustrated magnetism (25, 31), and topological physics (32, 33). Importantly, 1D and 2D atomic emitter arrays have been proposed to be topologically protected systems, where the photon propagation is robust against large imperfections while losses associated with free space emission are strongly suppressed (34–36). The array of capabilities of atom–2D photonics systems provides building blocks for realizing exotic quantum many-body systems complementary to, for example, ultracold atoms in optical lattices that rely solely on atomic contact interactions and tunneling (37).

Here, we discuss design, fabrication, and characterization of versatile 2D photonic structures tailored for atom–photon coupling. The particular platform of interest here is the 2D photonic crystal slab, where a periodic spatial modulation in dielectric defects distribution is arranged over a dielectric slab. The properties of a photonic crystal can be exploited to provide subwavelength-scale optical trapping and dispersion engineering (24, 38, 39). In this article, we present two distinct types of 2D photonic crystal slabs demonstrating photonic properties, such as directional spontaneous emission, spontaneous emission suppression, engineering of coherent atom–atom interactions, and topological properties in linear dielectric systems. Optical trapping schemes for trapping neutral ultracold Cs atoms in the vicinity of the photonic crystal slabs are also devised.

The 2D photonic crystal slabs are fabricated using electron beam lithography and standard etching processes, as reported in ref. 40, with a single suspended device layer of silicon nitride (SiN). They provide sufficient optical access to enable application of laser cooling and trapping techniques, such as a magneto-optical trap (MOT) and an optical dipole trap in close vicinity to the photonic crystal structures. An overview of our photonic

## Significance

**Specialized 2D photonic crystals have been developed to interact with ultracold atoms, which are identical particles demonstrating quantum behavior both in their interaction with photons and in their motional degrees of freedom. In the system presented here, the quantum nature of atoms is complemented with capabilities of 2D photonic crystals to engineer optical dispersion, light emission patterns, and photon-mediated coherent interactions. The combined system enables atom–atom interactions mediated by photons in the guided modes of the photonic crystals to provide additional tools to engineer quantum many-body systems and create exotic quantum matter.**

Author contributions: S.-P.Y., J.A.M., C.-L.H., and H.J.K. designed research; S.-P.Y., J.A.M., C.-L.H., and H.J.K. performed research; S.-P.Y. and J.A.M. contributed new reagents/analytic tools; S.-P.Y. and J.A.M. analyzed data; and S.-P.Y., J.A.M., C.-L.H., and H.J.K. wrote the paper.

Reviewers: A.B., University of Ottawa; and H.P., Harvard University.

The authors declare no conflict of interest.



[1]S.-P.Y. and J.A.M. contributed equally to this work.

[2]To whom correspondence may be addressed. Email: hjkimble@caltech.edu.

Published online June 12, 2019.

crystal devices is shown in Fig. 1*A*, where on-chip waveguides are connected to conventional optical fibers for efficient addressing to the guided modes of the 2D PhC slab by means of a self-collimation scheme (39, 41, 42). This enables direct optical characterization of their properties. The two types of lattice structure presented here are a square lattice of circular holes, shown in Fig. 1*B*, where we explore the anisotropic emission of excited-state atoms into the guided photonic modes, and a triangular array of hexagonal holes, depicted in Fig. 1*C*, where we focus on configurations with atomic resonances in the photonic band gap.

## Engineering Atom–Photon Interactions

The two photonic crystal slab structures display different regimes for light–matter interactions. For both designed structures, we use numerical tools to investigate how light–matter interactions are affected by the presence of the patterned dielectric.

We design the photonic crystals by specifying the unit cell geometry and then computing the band structures using a finite-element method (FEM). The parameter space defining the geometries is explored for useful optical properties such as a flat landscape of group velocities and opening of photonic band gaps, while satisfying practical requirements such as minimum feature sizes and mechanical robustness. The classical electromagnetic Green's tensor is then calculated using finite-difference time-domain (FDTD) methods on a simulated finite-size photonic crystal slab. Finally, further properties such as the emission characteristics of a dipole near the crystal can be obtained from the Green's tensor (43–45).

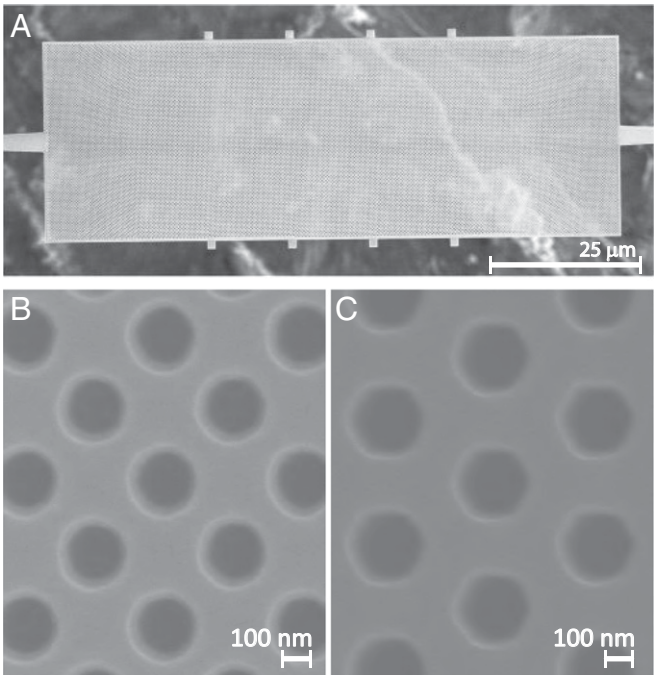


**Fig. 1.** A suspended 2D PhC slab for atom–light interactions. (*A*) SEM image of a photonic crystal slab structure, suspended by two single-beam SiN waveguides on left and right edges and released from the substrate for trapping and coupling with cold atoms directly transported from free space (Fig. 5 and Fig. 5 legend). The slab contains multiple sections with smoothly varying crystal parameters for guiding purposes (Fig. 6 and Fig. 6 legend). The dielectric tabs spaced along the top/bottom of the slabs delineate the boundaries between such sections. Irregular pattern in the background is an aluminum stage for the SEM, seen through a through-window of the chip. (*B* and *C*) Zoom-in SEM image of the square lattice of circular holes (*B*) and triangular lattice of hexagonal holes photonic crystals (*C*).

The LDOS can be written in terms of the imaginary part of the electromagnetic Green's tensor evaluated at the location of the dipole source itself, $\mathrm{Im}(\mathbf{G}(\vec{r},\vec{r},\nu))$. The atomic decay rate from an optically excited state $|j\rangle$ can be expressed in terms of the imaginary Green's tensor as (43, 45–47)

$$\Gamma_{\mathrm{Total}} = \frac{8\pi^2\mu_0}{\hbar}\cdot\sum_i \nu_{ij}^2 \mathrm{Tr}\left[D_{ij}\cdot \mathrm{Im}(\mathbf{G}(\vec{r},\vec{r},\nu_{ij}))\right], \qquad [1]$$

where $\nu_{ij}$ stands for the transition frequency between the excited state $|j\rangle$ and the ground state $|g_i\rangle$, $D_{ij} = \langle g_i|\,\hat{\vec{d}}^{\dagger}\,|j\rangle\,\langle j|\hat{\vec{d}}|g_i\rangle$ stands for the transition dipole matrix between the states in consideration, and the summation is over all ground states $|g_i\rangle$. To mediate atom–atom interactions using guided mode light, atoms in the vicinity of the photonic structure need to preferentially emit photons into the guided modes of the photonic crystal, instead of emitting into free space or other loss channels. Such performance can be characterized by the ratio $\Gamma_{2D}/\Gamma'$, where $\Gamma_{2D}, \Gamma'$ are the atom decay rates into the guided modes of interest and into any other channels, respectively, such that $\Gamma_{\mathrm{Total}} = \Gamma_{2D} + \Gamma'$. It is then useful to design structures that maximize the ratio $\Gamma_{2D}/\Gamma'$.

The richness of a 2D structure manifests when studying the spatial profile of the emitted electric field by an atomic dipole near the PhC slab. For example, in the presence of a band gap, the field produced by the dipole excitation is highly localized but yet inherits the symmetry of the dielectric pattern. If the dipole frequency lies outside a band gap and thus radiates into the propagating guided modes, highly anisotropic emission can be observed over select frequency ranges (29, 30, 48). Furthermore, the vector character of the guided-mode electric field and the tensor components of the atomic electric dipole operator can further affect the spatial emission pattern.

Our structures were designed to engineer interactions between Cs atoms and the transverse-electric (TE)-like guided modes, where the electric field is polarized predominately along the plane of the slabs. Due to the spin–orbit coupling in the first excited state, Cs has two families of optical transitions, marked by $\mathrm{D}_1$ and $\mathrm{D}_2$ lines, respectively, that can be used for optical trapping and studying light–matter interactions. The crystal dimensions are chosen such that the frequencies at high-symmetry points are aligned to the Cs $\mathrm{D}_1$ and/or $\mathrm{D}_2$ transitions at 335 THz (894 nm) and 351 THz (852 nm), respectively. We have thus far constrained our design to be based on a 200-nm-thick silicon nitride slab, given its low optical loss at near-infrared range and suitability for lithography and mechanical stability.

**Anisotropic Spontaneous Emission in a Square Lattice Photonic Crystal Slab.** We first consider a PhC slab consisting of a square lattice of circular holes, as shown in Fig. 1*B*. The geometry has lattice constant $a = 290$ nm, hole radius $R = 103$ nm, thickness $t = 200$ nm, and refractive index $n = 2$. This set of parameters was chosen to allow both Cs $\mathrm{D}_1$ and $\mathrm{D}_2$ lines to couple to a TE-like guided band. Specifically, Cs $\mathrm{D}_2$ resonance crosses a region of flat dispersion near the $X$ point, as shown in Fig. 2*A*. In $\vec{k}$ space, the dispersion relation $\nu(\vec{k})$ shows the effects of the dielectric patterning on the PhC as seen in Fig. 2*B*, which manifest as equi-frequency curves (EFCs) of constant guided-mode frequencies. The group velocity $\vec{v}_g = 2\pi\nabla_{\vec{k}}\nu(\vec{k})$ is perpendicular to the EFC that passes through a given $\vec{k}$. As marked in Fig. 2*B*, there is a region in $\vec{k}$ space where the EFCs are approximately linear, around $\nu = 390$ THz, indicating that the group velocity points in the same direction (i.e., along $\vec{k}_{\Gamma M}$ as in Fig. 2*B*). Therefore, all excitations with those wave vectors propagate approximately in the same direction. This gives rise to a

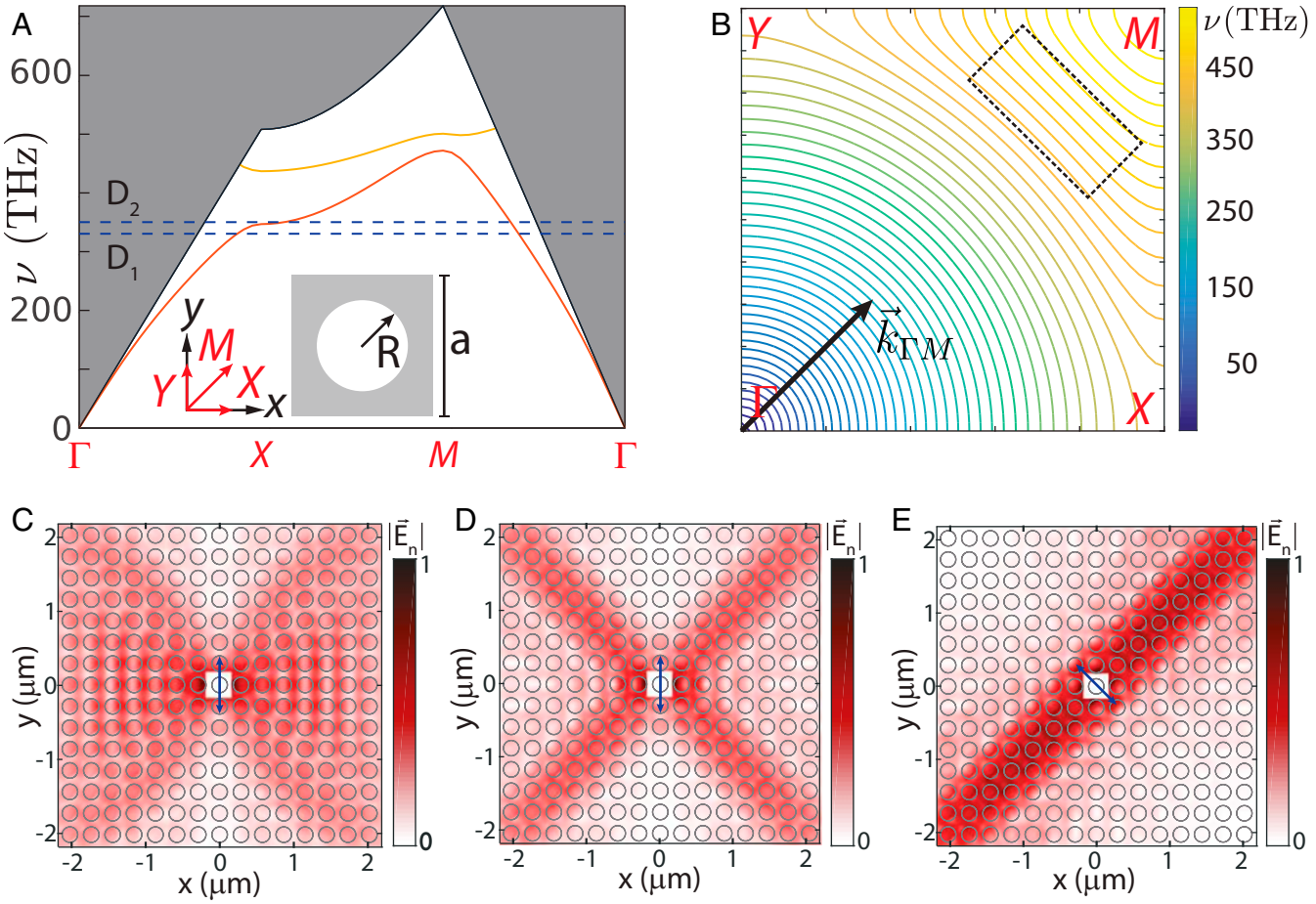


**Fig. 2.** Anisotropic spontaneous atomic emission in a square lattice of holes in a dielectric slab. (*A*) The reduced band structures for a unit cell with lattice constant $a = 290$ nm, hole radius $R = 103$ nm, thickness $t = 200$ nm, and refractive index $n = 2$. Dashed lines mark Cs $D_1$ and $D_2$ transition frequencies. *A*, *Inset* shows the real space (black arrows) and momentum space (red arrows) basis vectors. (*B*) EFCs in momentum space for the lowest band shown in *A*. The dashed black rectangle shows the region with parallel $\vec{v}_g$, around $\nu = 390 \pm 20$ THz. The $\vec{k}_{\Gamma M}$ direction is indicated. (*C*–*E*) Electric-field modulus $|\vec{E}_n|$, from a dipole at the center of the unit cell, normalized after removing the field in the immediate vicinity of the dipole, for three different situations. The dipole position and polarization are indicated by the blue arrows. In *C*, the dipole frequency is $\nu = 320$ THz, and the pattern has weak directional features. When the emission frequency is at $\nu = 390$ THz, the pattern is clearly directional, showing propagation along all $\vec{k}_{\Gamma M}$ directions. In *D*, the dipole is polarized along the *y* direction and emits along both diagonal directions. However, if the dipole is polarized along the diagonal direction, as in *E*, only one branch remains.

self-collimation effect (38, 49) that leads to directional emission (29, 30, 48, 50, 51).

In Fig. 2 *C*–*E* we study the effect of engineered band structure on the dipole emission pattern, using the EFC as a guide. We consider a dipole placed at the center of a hole, polarized parallel to the slab. For a dipole radiating at $\nu = 320$ THz and polarized along the $y$ direction, as in Fig. 2*C*, the radiation pattern is roughly isotropic and no preferred direction is found. However, if the radiation frequency is at $\nu = 390$ THz, as in Fig. 2*D*, a clear directional component along $\vec{k}_{\Gamma M}$ is present. Both branches are present due to the dipole polarization and folding symmetry of the square lattice. Finally, we can select a single branch by polarizing the dipole along the diagonal direction, as shown in Fig. 2*E*. We note that by changing the lattice constant to 330 nm, the center frequency of the flat dispersion region in the lattice momentum space will correspond to the Cs $D_2$ line transition frequency at 351 THz.

**Engineering Atom–Light Interaction in a Triangular Lattice Photonic Crystal Slab.** A photonic crystal with a triangular lattice of hexagonal holes was designed to create a band gap for the TE-like modes. As indicated in Fig. 3*A*, we parameterize the photonic crystal unit cell by its lattice constant $a$ and the width $t$ of the dielectric tether separating adjacent holes. The unit cell geometry and the band structure for $a = 405$ nm and $t = 180$ nm are plotted in Fig. 3*A*. The TE band gap spans a frequency range from the $K$ point at the lower band to the $M$ point at the higher band and covers the range of Cs $D_1$ and $D_2$ frequencies. We now study the emission properties of dipole excitation in the vicinity of the photonic crystal slab, by calculating the Green's tensor in the hole center of a unit cell of a photonic crystal slab (Fig. 3*B*). The TE band gap efficiently suppresses emission of a dipole emitter in its frequency range. Numerical simulations show that for the two in-plane polarizations, a suppression of up to 8 dB on the spontaneous emission rate can be achieved. This behavior does not manifest in structures such as the square lattice of holes discussed before, where there is not a complete TE-like band gap. Here we note that $G_{xx} = G_{yy}$ is due to threefold rotation symmetry of the lattice. The minor differences between the $x$ and $y$ traces are likely numerical artifacts associated with the simulation volume. $G_{zz}$ is not affected by the TE band gap, demonstrating instead a smooth profile within the simulated bandwidth that varies primarily with the slab thickness. This is because the $z$-polarization direction corresponds principally to a TM guided mode. We also note that multiple Fabry–Perot resonances are manifest in $G_{xx}$

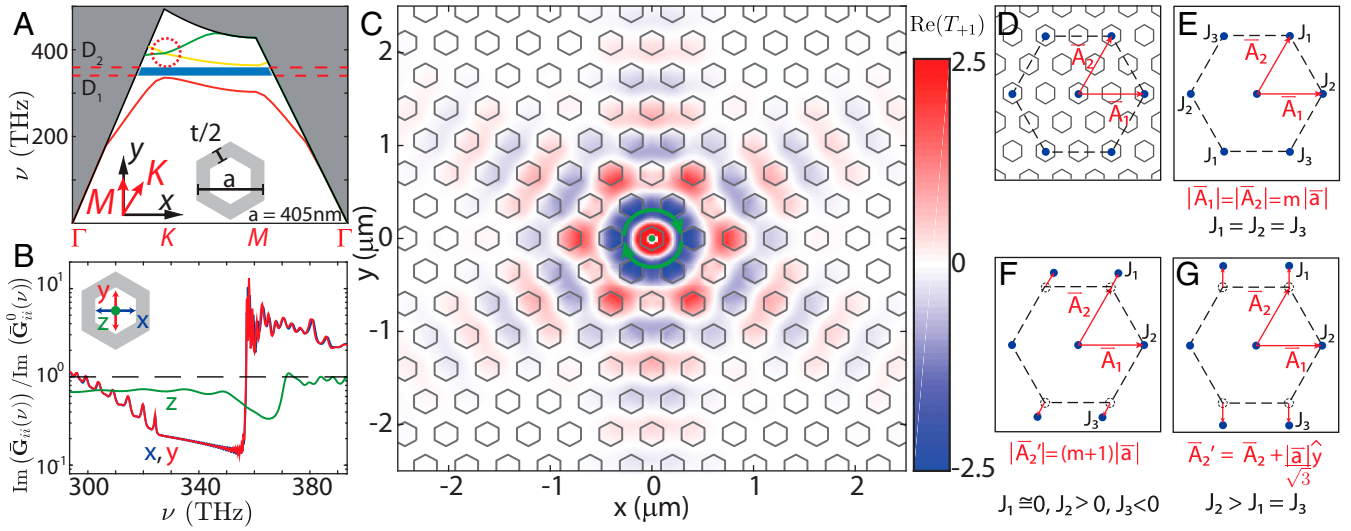


**Fig. 3.** Engineering atom–light interaction in a band gap of a triangular lattice of hexagonal holes in a dielectric slab. (*A*) The reduced band structure of the hexagonal lattice photonic crystal. A 2D TE-like band gap (blue shaded area) manifests between the top of the lower band (red) and the bottom of the higher bands (green, yellow). The dashed red circle indicates a crossing at the *K* point between higher bands (Fig. 4*A*). (*B*) The imaginary component of the Green's tensor, $\mathrm{Im}(\mathbf{G}_{ii}(\vec{r},\vec{r},\nu))/\mathrm{Im}\left(\mathbf{G}^0_{ii}(\vec{r},\vec{r},\nu)\right.$, normalized by the free-space tensor components, $i$ = x (blue), y (red), z (green). *B*, *Inset* shows the excitation dipole position and polarization. (*C*) The real part of the Green's tensor component $\mathrm{Re}(T_{+1}(\vec{r},\nu_0))$ in unit of the decay rate $\Gamma_{\mathrm{Total}}$. The excitation frequency, $\nu_0$, is placed in the middle of the band gap. The green dot indicates the position of the emitting dipole, while the green arrows indicate its polarization. (*D*) A superlattice of atoms associated with lattice vectors $\vec{A}_1, \vec{A}_2$ is formed by placing atoms in selected sites in the photonic crystal. (*E–G*) The following interaction parameters $J_i$ can be engineered: (*E*) $J_1 = J_2 = J_3$, with $J_i = -0.40\Gamma_{\mathrm{Total}} < 0$ for $m_{11} = m_{22} = m = 3$, and $J_i = 0.11\Gamma_{\mathrm{Total}} > 0$ for $m = 4$; (*F*) lengthening the $\vec{A}_2$ vector by one unit lattice vector from the $m = 4$ case results in $J_1 = -0.02\Gamma_{\mathrm{Total}} > 0$, $J_2 = 0.10\Gamma_{\mathrm{Total}} > 0$, $J_3 = -0.10\Gamma_{\mathrm{Total}}$, which has a weak coupling to the $J_1$ site, forming an effective square-lattice–like interaction; and (*G*) stretching the superlattice perpendicularly to $\vec{A}_1$ from the $m = 2$ case creates an anisotropic interaction of $J_2 = 1.31\Gamma_{\mathrm{Total}}$ while $J_1 = J_3 = 0.27\Gamma_{\mathrm{Total}}$.

and $G_{yy}$ near the edges of the band gap in Fig. 3*B*. This is due to finite reflection at the boundaries of the simulated finite-size PhC, which is terminated abruptly into a uniform dielectric background.

The excitation field pattern in the TE-like band gap is plotted in Fig. 3*C*. The modes created by the dipole emitter are non-propagating modes that are confined in the vicinity of the dipole in an evanescent manner. It was proposed that evanescent modes surrounding an atom can be exploited to create a coherent interaction between adjacent atoms with the interaction terms (11, 23, 24, 52, 53)

$$J_{pq} = \frac{4\pi^2\mu_0\nu_{ij}^2}{\hbar} \cdot \mathrm{Tr}\left[D_{ij} \cdot \mathrm{Re}(\mathbf{G}(\vec{r}_p, \vec{r}_q, \nu_{ij}))\right], \qquad [2]$$

where $D_{ij}$ is the dipole matrix as defined previously, and now the Green's tensor evaluated at the $p$th atom position generated by the dipole of the $q$th atoms $\mathbf{G}(\vec{r}_p, \vec{r}_q)$ is considered. The evanescent guided modes of the photonic crystal mediate atom–atom interactions with the Hamiltonian,

$$\hat{H}_I = \sum_{pq} J_{pq}\sigma_{ij}^p\sigma_{ji}^q, \qquad [3]$$

where $\sigma_{ij}^p = |g_i\rangle^p \langle j|^p$.

This interaction Hamiltonian forms a coupled system for atoms $p$ and $q$ with transition between the states $|g_i\rangle$ and $|j\rangle$. For simplicity, the following discussion focuses on a two-state atom system. As an example, such a two-state system can be realized in our photonic crystal platform with Cs atoms constrained in the $|F = 4, m_f = 4\rangle$ to $|F' = 5, m_f' = 5\rangle$ transition. Writing the Green's tensor in its spherical components in Eq. **2**, only the term $T_{+1}(\vec{r},\nu) = (\hat{e}_+ \cdot \mathbf{G}(\vec{r},\vec{r}_0,\nu) \cdot \hat{e}_-)$ is nonzero through the trace operation, where $\hat{e}_\pm = \frac{\hat{x} \pm i\hat{y}}{\sqrt{2}}$ and $\vec{r}_0$ is the position of the emitting dipole. The term is calculated numerically from the counterclockwise circular component of the electric field $\hat{e}_+ \cdot \vec{E}$ generated by a clockwise circular dipole source $p\hat{e}_-$ placed at the origin, $\vec{r}_0$. The profile of $\mathrm{Re}(T_{+1}(\vec{r},\nu_0))$, with $\nu_0$ within the bandwidth of the 2D TE band gap, is plotted in Fig. 3*C*, in units of the decay rate $\Gamma_{\mathrm{Total}}$.

The geometric pattern of the Green's tensor $\mathrm{Re}(\mathbf{G})$ can be exploited to engineer the form of the interaction Hamiltonian. The relative position of atoms on the photonic crystal determines the sign and strength of the atom–atom interaction as facilitated by the evanescent field pattern. Assuming a site-wise controlled placement of atoms can be realized with a technique like the optical tweezers (54), atoms can be assembled into a superlattice on the photonic crystal to form a quantum many-body system with the desired atom–atom interaction. We define such a superlattice by lattice vectors spanned by integer multiple combinations of the base lattice vectors, $\vec{A}_i = m_{ij} \cdot \vec{a}_j$. In Fig. 3 *D–G* we investigate this capability by identifying configurations that would create nearest-neighbor coupling of controlled sign and engineered anisotropy.

It is worth noting that the band structure of the triangular PhC enables reliable creation of symmetry-protected, purely circularly polarized mode pockets in a hexagonal lattice structure. The mode crossing in the two upper bands at the $K$ point, encircled in red in Fig. 3*A*, is a degeneracy that is protected by the sixfold rotation symmetry of the lattice (55) around the $z$ axis perpendicular to the device plane. This degeneracy can be lifted by perturbing the unit cell dielectric distribution, while preserving a threefold rotation symmetry, as shown in Fig. 4 *A* and *B*. At high-symmetry points, such as the center of the hole, the guided-mode field pattern is necessarily purely circularly polarized. Any defined in-plane linear direction is incompatible with the threefold rotation symmetry. The circular polarization persists around the $K$ point with gradually reducing purity in a bandwidth comparable to the splitting of the degeneracy. In Fig. 4 *C–F* we plot the field profiles and their circular

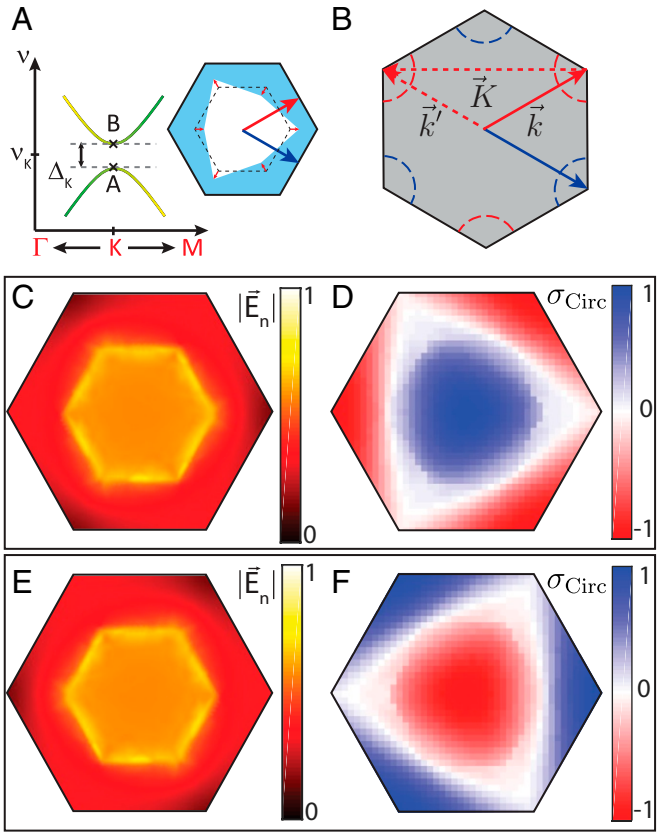


**Fig. 4.** Lifting the degeneracy at the *K* point to create symmetry-protected, circularly polarized mode pockets. (*A*) A modified unit cell for the hexagonal photonic crystal where the vertices of the hole are moved to break the mirror symmetry in the *K* direction while maintaining threefold rotation symmetry around its center. Such deformation lifts the degeneracy of the two upper bands at the *K* point plotted in Fig. 3*A*. (*B*) A guided mode of the photonic crystal with $\vec{k}$ lying on the *K* point of the Brillouin zone maintains the threefold rotation symmetry, as such rotation operation transforms the momentum vector onto $\vec{k}' = \vec{k} + \vec{K}$, where $\vec{K}$ is a lattice momentum, and $\vec{k}$ and $\vec{k}'$ are equivalent. *C* and *D* show the electric field pattern $|\vec{E}|$ and circular polarization ratio, $\sigma_{Circ}$ for point A in the dispersion plot in *A*, for a unit cell with vertices shifted by 2.5 nm, lifting the degeneracy at $\nu_K = 387.6$ THz by $\Delta_K = 0.7$ THz. *E* and *F* show the corresponding plots for point B in *A*. We note that the modes have a strong electric field in the center of the hole with purely circular polarization.

polarization fraction, defined as $\sigma_{Circ} = \frac{I_{CCW} - I_{CW}}{I_{CCW} + I_{CW}}$, where $I_{CW}, I_{CCW}$ are the local intensities of clockwise and counterclockwise polarizations.

To respect time-reversal symmetry, the $K$ points of opposite momenta in Fig. 4 have opposite circular polarization in the plane of Fig. 4. Furthermore, because of threefold symmetry, the TE-like guided modes at three $K$ points, each separated by 120°, have the same sense of polarization circulation relative to the axis perpendicular to the PhC; guided modes at the $K$ points on the other triad (rotated by 60°) have the opposite sense of polarization circulation. Adding a quantum emitter, such as a trapped atom to the center of the unit cell, can create selective coupling to either of the $K$-point triads, reminiscent of chiral light–matter interaction in the 1D case (56). In our 2D PhC, atomic emission with $\Delta m_f = 1$ should couple to the $K$ points in one triad and transition with $\Delta m_f = -1$ will emit along the other triad of $K$ points. By selectively coupling the guided modes with trapped atoms polarized at a certain magnetic sublevel $m_f$, one can potentially create topological properties while using linear dielectric media (33, 35).

## Optical Trapping Schemes

Here we present an optical loading and trapping scheme for atoms in close proximity to the 2D photonic crystal. The method is based on a blue-detuned optical "conveyor belt" technique (13, 24, 38, 57) (Fig. 5), where a set of counterpropagating beams forms a moving standing-wave optical trap. The calculations have been carried out for both structures described earlier. First, we consider the case of a single linearly polarized beam, near detuned with respect to the Cs $D_2$ wavelength, incident normally to the slab plane, as in Fig. 5*A*. The reflection from the dielectric creates a strong intensity modulation as shown in Fig. 5 *B* and *C*. Near the center of the hole, a local intensity minimum is present and can be used to localize cold atoms. It is also possible to trap above the structure on several intensity maxima, using red-detuned light.

The blue-detuned trap is favored over the conventional red-detuned trap due to the fact that optical intensity tends to sharply increase near subwavelength features in the dielectric structure as a result of near-field effects. A blue-detuned trap with such an intensity pattern would then create a strong potential barrier near the dielectric surface to prevent untrapped atoms from crashing into the dielectric structures (24, 38). The same mechanism also prevents trapped atoms from coming into close vicinity of dielectric surfaces, where the Casimir–Polder force (24, 45, 58) becomes dominant. Cs accumulation on the devices was found

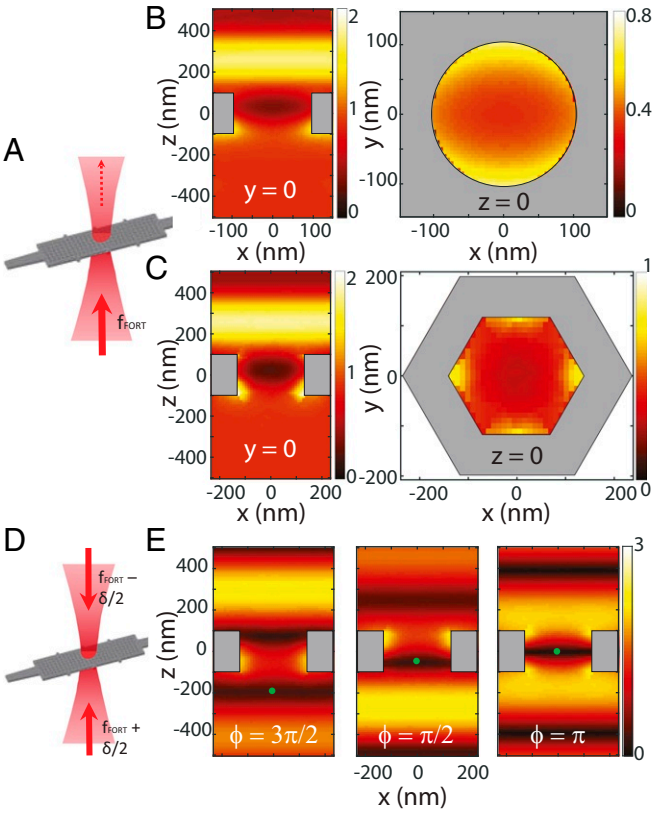


**Fig. 5.** Optical dipole traps near the PhC slab. (*A*–*C*) A linearly polarized beam is sent with wave-vector $\vec{k}$ normal to the plane of the slab (*A*), forming local intensity minima for both the square lattice (*B*) and the hexagonal lattice (*C*) structures. *B* and *C*, *Left* and *Right* show intensity cross-sections in the $x-z$ and $x-y$ planes, for $y = 0$ and $z = 0$, respectively, as indicated. (*D*) An optical conveyor belt can be formed by using near-detuned counterpropagating beams. (*E*) For different relative phases between the beams the intensity pattern displaces its intensity minimum (green circles) into the vacuum spaces. Here the triangular structure is depicted. Relative phases are indicated in each panel.

to be the primary limitation of device lifetime in previous experiments with cesium near nanostructures (9, 10). We suggest that this could be alleviated with blue-detuned traps.

To perform an optical conveyor belt, a moving 1D optical lattice can be formed using two linearly polarized, counterpropagating laser beams, with a relative detuning $\delta$ and incident normally with respect to the device plane, as shown in Fig. 5*D*. The lattice can be loaded with cold atoms from a conventional free-space MOT sufficiently far from the nanostructure and can be continuously moved into and through the device layer at a rate controlled by the detuning $\delta$. To provide transverse confinement in such a blue-detuned 1D lattice, additional beams can be used that do not alter this discussion significantly. Fig. 5*E* shows the trap pattern for different relative phases between the beams. Confinement in the additional $y$ direction is guaranteed as seen in $xy$ patterns in Fig. 5 *B* and *C*. It is possible to extract information of the phase of the moving lattice, hence inferring the position of the loaded atoms, by imaging the scattering of the device layer or collecting light from the device through an outcoupling port (13). Moreover, since a single incident beam can already form a local trap intensity minimum within the hole, it is possible to abruptly turn off one of the two beams as the intensity node of the blue lattice passes through the device layer to convert the conveyor belt directly into a localized trap. Further schemes using guided modes to create traps can be investigated, as suggested in ref. 24.

Using optical tweezers in 2D PhC systems is a powerful alternative. Recent development of optical tweezers techniques as used in refs. 6, 12, and 59–61 allows for precise and dynamic placement of multiple atoms. The optical access of our chip configuration, as well as the planar geometry of the 2D photonic crystal slab, is compatible with optical tweezers techniques. In the near term, controlled placement of pairs of atoms in determined relative positions could be achieved, as a means to directly characterize the anisotropic interactions described previously. Ultimately, an array of atoms could be arranged in a superlattice on the photonic crystal with multiple optical tweezers to engineer quantum many-body systems with controlled interactions.

Finally, we note that surface potentials are relevant for trapping at short distances ($\sim$100 nm) from the dielectric surface. The precise calculation of these potentials is outside the scope of this work, but we refer to similar work where these potentials have been calculated or included in trajectory simulations near dielectric structures, as in refs. 4, 7, 10, 13, 24, 62, and 63. As seen in the transverse profile for the trapping potentials in Fig. 5 *B* and *C*, with modest intensity it is possible to overcome short-range attractive surface potentials.

The research reported in this paper could potentially impact current research on atom–surface interactions; see, for example, ref. 64 for a review on current advances on these topics. Different sets of experiments have investigated the effects on atomic line shifts and decay rate modifications for atoms near surfaces, in different microscopic geometries, which are relevant to our system. Spectral distortion for Cs atoms induced by surface forces has been measured in thermal atomic vapor (65–67). In the nanophotonics domain, surface effects on atomic trajectories for thermal (300 K) and cold atoms ($<$1 mK) have been recently reported in different experimental settings, such as nonpatterned waveguides (63), and microtoroids (7, 62), nanofibers (2, 4), and photonic crystal waveguides (9–13), respectively. Although the dielectric surfaces will have a significant effect on the motional and radiative atomic properties, all of the reported experimental results are supported by the numerical simulations.

**Device Characterization.** We fabricate the 2D PhC devices using a similar process to that presented in ref. 40. The photonic crystal slab is suspended atop a through-window chemically etched through the silicon substrate and is connected to the chip substrate via a set of silicon nitride waveguides and tethers. The waveguides can be efficiently coupled to conventional single-mode optical fibers using the method developed in ref. 68. We then connect these waveguides of 500 nm width to the 2D photonic crystal slab by using a 1:10 linear taper to gradually enlarge the waveguide width to 8 μm. The function of the linear taper is twofold: Optically, it widens the optical mode profile from subwavelength to several micometers. As the guided mode enters the 2D structure, the widened mode profile suppresses the spread in the transverse k component of the optical mode, so that it can couple into a 2D photonic crystal mode of a well-defined lattice momentum vector. Mechanically, the widening taper distributes the high tensile stress carried on the waveguide evenly onto the larger, more rigid 2D photonic crystal slab, hence improving device yield. We have fabricated fully suspended 2D PhC slabs with a size up to 30 μm $\times$ 90 μm with high ($>$90%) yield (39).

For the 2D system in consideration, optical input can be introduced into the crystal from a continuum of directions in the device plane. This is achieved in our system by maintaining the input waveguide configuration, but rotating the lattice vectors of the 2D PhC. Typically, each chip contains 16 devices, and a gradual rotation of the crystal lattices across the devices allows studying the device's response to input light in quasi-continuous directions. We found it to be most informative to characterize these devices from the high-symmetry directions of the Brillouin zone, as this provides direct information of the frequencies of the upper and lower bands at these directions. For the case of the hexagonal crystal, the TE-like band gap exists between the frequencies of the lower band of the $K$ point and the higher band of the $M$ point. Direct measurement of these frequencies allows us to infer the frequency range of the 2D photonic band gap.

A set of measured device transmission and reflection spectra is plotted in Fig. 6, with FDTD simulation traces for comparison. The simulations of devices were carried out using identical photonic crystal parameters, but with reduced device size, due to limits of computational resources. Spectral features such as stop bands and resonance dips can be identified in simulation and measured traces with good correspondence. In the experimental measurements, residual reflection from supporting structures on the waveguide far from the PhC section create a percent-level reflection that interferes with the PhC signal, resulting in the dense interference fringes seen on the reflection traces in Fig. 6 *A* and *C*. These fringes are not intrinsic to the photonic crystals and can be alleviated using a single row of holes that provide an effective AR coating (38, 69). In addition to observing the band edges of the high-symmetry directions, useful information regarding the PhC can be inferred from the various features on the transmission and reflection spectra.

We focus our attention on the band edges, where the frequency of input light changes from propagation band to band gap. Fig. 6 *A* and *B* shows the comparison between measurements and numerical simulations, respectively, for the lower band edge at the $X$ point of the square lattice. The TE band gap in the $X$ orientation prevents transmission of the TE-like mode above about 348 THz. Also, the reflection increases rapidly above this frequency.

Fig. 6 *C* and *D* depicts transmission and reflection spectra of a hexagonal photonic crystal in the $M$ direction. The TE band gap of the hexagonal photonic crystal creates an abrupt suppression of transmission. We observe a set of resonances with reducing frequency spacing as the frequency approaches the band edge. These resonances result from reflection at the boundaries of the photonic crystal, and the reduction of resonance spacing resulted

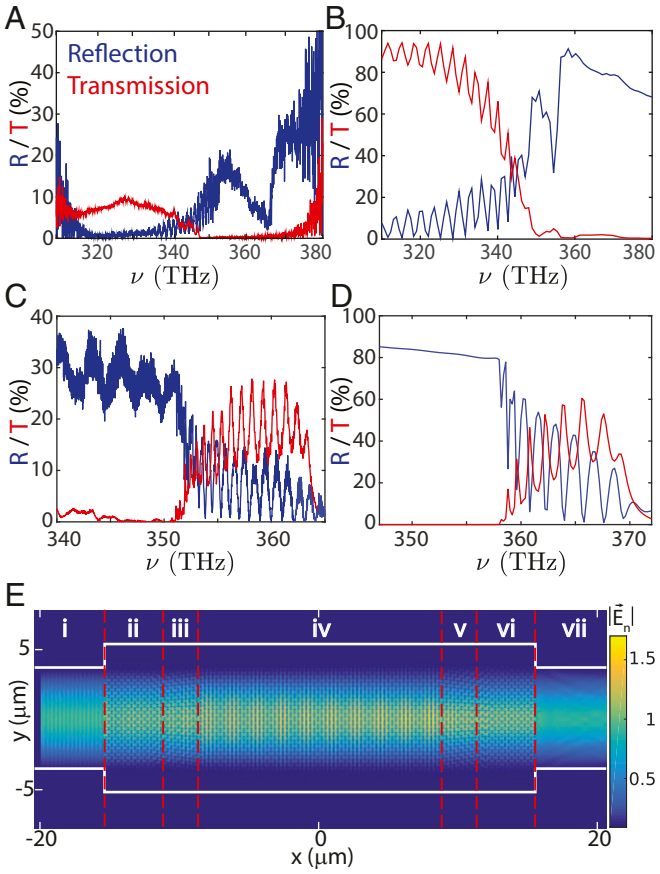


**Fig. 6.** Device characterization. (*A* and *B*) For a square lattice, the comparison between measured (*A*) and simulated (*B*) reflection and transmission traces reveals some common features. (*C* and *D*) For the hexagonal lattice, the measured (*C*) and simulated (*D*) traces reflect the existence of a band gap. We note that the total device lengths in the simulated devices are shorter, due to computational resource limits, resulting in a larger frequency spacing between the resonances. Additionally, the measured traces in Fig. 6 include coupling losses between the fiber and the PhC section, resulting in the lower overall signal level compared with the theoretical traces. The small shift in resonance frequencies between reflection and transmission traces in *C* resulted from an oxygen plasma cleaning process carried out between the two measurements. (*E*) Simulated field intensity for an incident guided mode, $|\vec{E}_n|$, coming through the left waveguide and propagating through the crystal near the Cs $D_2$ line. White lines indicate the device contour. Multiple photonic sections are divided by the dashed red lines. *i* and *vii* are the input/output 8-μm rectangular waveguides; *ii* and *vi* are the self-collimation regions with the $\Gamma-M$ direction aligned along the horizontal axis; *iii* and *v* are the transition sections to align the self-collimated light at Cs $D_2$ frequency to the *M* point of the PhC in *iv*. Note the incoming waveguide mode does not diverge as it enters the crystal from the left.

from increasing group index of the guided mode, similar to the 1D case (40). The reduction of contrast of the resonances as the frequency approaches the band edge results also from the increased group index, which creates enhanced field buildup inside the photonic crystal and enhances scattering into other modes of the 2D photonic crystal slab (70).

Furthermore, from these numerical simulations it is possible to study the field profile as it propagates along the device as in Fig. 6*E* for frequencies in the Cs $D_2$ line. To avoid a divergence of the input mode, the nominal PhC is placed between two self-collimation sections where the unit cells are aligned such that at the frequencies of interest, the group velocity points along the left–right direction; that is, the $\vec{k}_{\Gamma M}$ is oriented along the $x$ direction in Fig. 6*E*, as discussed before (38, 49). This self-collimation section has lattice constant $a_{SC} = 330$ nm and radius 103 nm. The nominal section in this case consists of a unit cell lattice constant of 360 nm and a hole radius of 105 nm. These dimensions place the Cs $D_2$ frequency near the $M$ point of the lower band.

**Outlook.** In this article, we have described a collection of components and capabilities that will allow experiments with cold atoms in 2D photonic crystal systems (24, 25). Photonic crystals can indeed be built to produce the desired band structures near cesium resonances. Corresponding devices have been fabricated reliably using well-understood processes, and the expected optical features in reflection and transmission spectra have been verified (39). The Green's tensor calculations show that a wide variety of atom–light interactions can be engineered, including enhancement and suppression of decay rates, directional propagation, and finite-range atom–atom interactions mediated by photons. An optical trapping and loading scheme has been proposed to allow placement of atoms in positions in the crystal structures to demonstrate the suggested phenomena. In the foreseeable future, we should take several steps to further verify the properties of the devices with atoms. The loading and trapping of atoms using the optical conveyor belt, which has been demonstrated in 1D PhC waveguides (13), should allow demonstration of enhanced or suppressed atomic decay rates corresponding to the Green's tensor results, which should be measurable with time-domain decay rate measurements with the integrated waveguides on the chip (10). Optical tweezers should then be deployed in our system to directly measure the predicted anisotropic interactions. Single-atom control near-nanophotonics waveguides have already been demonstrated using optical tweezers and conveyor belts (6, 12), paving the way to integrate these control techniques into 2D structures. Achieving these steps sequentially should steadily bring us toward realization of engineerable quantum many-body systems in our 2D photonic crystal devices.

## Materials and Methods

The photonic crystal band structures are simulated using the COMSOL Multiphysics 3.5a finite-element eigenvalue solver (71). A unit cell geometry is plotted, a Bloch boundary condition with lattice momentum $\vec{k}$ is specified for each simulation, and the eigenfrequencies are solved for each $\vec{k}$ along the high-symmetry directions to form the band structures.

The Green's tensor calculations are carried out using the MEEP package (72) and also Lumerical FDTD software (73). A finite-size photonic crystal slab is created in a 3D simulation volume, and a dipole source is placed in a desired location to provide excitation. For the decay rate enhancement, the imaginary component of the resulting field is recorded at the dipole position, and a Fourier transform is carried out to extract the frequency response. The resulting emission mode profile from the dipole source is also recorded for the anisotropic emission studies.

The optical trapping conveyor scheme is designed also with COMSOL Multiphysics 3.5a, where a single-frequency plane wave is injected onto a unit cell from a perpendicular orientation to compute the resulting field pattern. The electric field is then exported, parity reversed to create a counterpropagating wave, and superimposed with the forward-propagating mode to form a standing wave. A relative phase between the two modes is swept to create the conveyor motion.

The fabrication of devices starts with 200-μm-thick silicon substrates precoated with 200-nm stoichiometric silicon nitride on both sides by Silicon Valley Microelectronics. The waveguides and photonic crystals were defined using a Raith EBPG 5000+ lithography tool with a ZEON Chemicals ZEP520A electron beam resist and pattern transferred into a silicon nitride device layer using reactive ion etching with an Oxford PlasmaLab 100 tool with $C_4F_8$ and $SF_6$ chemistry. The silicon substrate through-hole etch is done using a potassium hydroxide solution and subsequent cleaning with a Cyan-Tek Nanostrip and 1:10 buffered hydrofluoric acid. The finished devices are brought out of liquid environment using critical point drying. The optical testing of devices is done by injecting broadband light from an InPhenix SLED light source into the device with a cleaved 780HP optical fiber, and the reflection spectrum is analyzed using an Anritsu MS9740A optical spectrum analyzer.

**ACKNOWLEDGMENTS.** We gratefully acknowledge discussions with Andrew McClung, Jonathan Hood, Lucas Peng, Xingsheng Luan, Alexander Burgers, Michael J. Martin, and Ana Asenjo-García from the Caltech Quantum Optics Group; and with Alejandro González-Tudela and Ignacio Cirac (Max Planck Institute of Quantum Optics, Garching). S.-P.Y. and J.A.M. acknowledge support from the International Fulbright Science and Technology Award. C.-L.H. acknowledges support from the Air Force Office of Scientific Research (AFOSR), Grant FA9550-17-1-0298 and the Office of Naval Research (ONR), Grant N00014-17-1-2289. H.J.K. acknowledges funding from ONR Grant N00014-16-1-2399, ONR Multidisciplinary University Research Initiatives (MURI) Quantum Opto-Mechanics with Atoms and Nanostructured Diamond Grant N00014-15-1-2761, AFOSR MURI Photonic Quantum Matter Grant FA9550-16-1-0323, the National Science Foundation (NSF) Grant PHY-1205729, and the NSF Institute for Quantum Information and Matter Grant PHY-1125565. H.J.K. also acknowledges the support of the Caltech Kavli Nanoscience Institute and the cleanroom facilities of O. Painter and his group, where device fabrication was carried out by S.-P.Y.

1. D. E. Chang, J. S. Douglas, A. González-Tudela, C.-L. Hung, H. J. Kimble, Colloquium: Quantum matter built from nanoscopic lattices of atoms and photons. *Rev. Mod. Phys.* **90**, 031002 (2018).
2. A. Goban *et al.*, Demonstration of a state-insensitive, compensated nanofiber trap. *Phys. Rev. Lett.* **109**, 033603 (2012).
3. G. Sagué, E. Vetsch, W. Alt, D. Meschede, A. Rauschenbeutel, Cold-atom physics using ultrathin optical fibers: Light-induced dipole forces and surface interactions. *Phys. Rev. Lett.* **99**, 163602 (2007).
4. E. Vetsch *et al.*, Optical interface created by laser-cooled atoms trapped in the evanescent field surrounding an optical nanofiber. *Phys. Rev. Lett.* **104**, 203603 (2010).
5. N. V. Corzo *et al.*, Large Bragg reflection from one-dimensional chains of trapped atoms near a nanoscale waveguide. *Phys. Rev. Lett.* **117**, 133603 (2016).
6. J. D. Thompson *et al.*, Coupling a single trapped atom to a nanoscale optical cavity. *Science* **340**, 1202–1205 (2013).
7. D. J. Alton *et al.*, Strong interactions of single atoms and photons near a dielectric boundary. *Nat. Phys.* **7**, 159–165 (2011).
8. J. Volz, M. Scheucher, C. Junge, A. Rauschenbeutel, Nonlinear $\pi$ phase shift for single fibre-guided photons interacting with a single resonator-enhanced atom. *Nat. Photonics* **8**, 965–970 (2014).
9. A. Goban *et al.*, Atom-light interactions in photonic crystals. *Nat. Commun.* **5**, 3808 (2014).
10. A. Goban *et al.*, Superradiance for atoms trapped along a photonic crystal waveguide. *Phys. Rev. Lett.* **115**, 063601 (2015).
11. J. D. Hood *et al.*, Atom–atom interactions around the band edge of a photonic crystal waveguide. *Proc. Natl. Acad. Sci. U.S.A.* **113**, 10507–10512 (2016).
12. M. E. Kim, T.-H. Chang, B. M. Fields, C.-A. Chen, C.-L. Hung, Trapping single atoms on a nanophotonic circuit with configurable tweezer lattices. *Nat. Commun.* **10**, 1647 (2019).
13. A. P. Burgers *et al.*, Clocked atom delivery to a photonic crystal waveguide. *Proc. Natl. Acad. Sci. U.S.A.* **116**, 456–465 (2019).
14. D. Englund, I. Fushman, A. Faraon, J. Vuckovic, Quantum dots in photonic crystals: From quantum information processing to single photon nonlinear optics. *Photonics Nanostruct. Fundam. Appl.* **7**, 56–62 (2008).
15. P. Lodahl, S. Mahmoodian, S. Stobbe, Interfacing single photons and single quantum dots with photonic nanostructures. *Rev. Mod. Phys.* **87**, 347–400 (2014).
16. G. Khitrova, H. M. Gibbs, Quantum dots: Collective radiance. *Nat. Phys.* **3**, 84–85 (2007).
17. R. N. Patel *et al.*, Efficient photon coupling from a diamond nitrogen vacancy center by integration with silica fiber. *Light Sci. Appl.* **5**, e16032 (2016).
18. A. Sipahigil *et al.*, An integrated diamond nanophotonics platform for quantum optical networks. *Science* **354**, 847–850 (2016).
19. M. Gündoğan, P. M. Ledingham, K. Kutluer, M. Mazzera, H. de Riedmatten, Solid state spin-wave quantum memory for time-bin qubits. *Phys. Rev. Lett.* **114**, 230501 (2015).
20. T. Zhong, J. M. Kindem, E. Miyazono, A. Faraon, Nanophotonic coherent light–matter interfaces based on rare-earth-doped crystals. *Nat. Commun.* **6**, 8206 (2015).
21. A. M. Dibos, M. Raha, C. M. Phenicie, J. D. Thompson, Atomic source of single photons in the telecom band. *Phys. Rev. Lett.* **120**, 243601 (2018).
22. P. Solano, P. Barberis-Blostein, F. K. Fatemi, L. A. Orozco, S. L. Rolston, Super-radiance reveals infinite-range dipole interactions through a nanofiber. *Nat. Commun.* **8**, 1857 (2017).
23. J. S. Douglas *et al.*, Quantum many-body models with cold atoms coupled to photonic crystals. *Nat. Photonics* **9**, 326–331 (2015).
24. A. Gonzalez-Tudela, C.-L. Hung, D. E. Chang, J. I. Cirac, H. J. Kimble, Subwavelength vacuum lattices and atom–atom interactions in two-dimensional photonic crystals. *Nat. Photonics* **9**, 320–325 (2015).
25. C.-L. Hung, A. González-Tudela, J. Ignacio Cirac, H. J. Kimble, Quantum spin dynamics with pairwise-tunable, long-range interactions. *Proc. Natl. Acad. Sci. U.S.A.* **133**, E4946–E4955 (2016).
26. M. T. Manzoni, L. Mathey, D. E. Chang, Designing exotic many-body states of atomic spin and motion in photonic crystals. *Nat. Commun.* **8**, 14696 (2017).
27. V. Paulisch, H. J. Kimble, A. González-Tudela, Universal quantum computation in waveguide QED using decoherence free subspaces. *New J. Phys.* **18**, 043041 (2016).
28. H. Pichler, S. Choi, P. Zoller, M. D. Lukin, Universal photonic quantum computation via time-delayed feedback. *Proc. Natl. Acad. Sci. U.S.A.* **114**, 11362–11367 (2017).
29. A. González-Tudela, J. I. Cirac, Quantum emitters in two-dimensional structured reservoirs in the nonperturbative regime. *Phys. Rev. Lett.* **119**, 143602 (2017).
30. A. González-Tudela, J. I. Cirac, Markovian and non-Markovian dynamics of quantum emitters coupled to two-dimensional structured reservoirs. *Phys. Rev. A* **96**, 043811 (2017).
31. J. Struck *et al.*, Quantum simulation of frustrated classical magnetism in triangular optical lattices. *Science* **333**, 996–999 (2011).
32. L. Lu, J. D. Joannopoulos, M. Soljačić, Topological photonics. *Nat. Photonics* **8**, 821–829 (2014).
33. T. Shi, H. J. Kimble, J. I. Cirac, Topological phenomena in classical optical networks. *Proc. Natl. Acad. Sci. U.S.A.* **114**, E8967–E8976 (2017).
34. A. Asenjo-Garcia, M. Moreno-Cardoner, A. Albrecht, H. J. Kimble, D. E. Chang, Exponential improvement in photon storage fidelities using subradiance and "selective radiance" in atomic arrays. *Phys. Rev. X* **7**, 031024 (2017).
35. J. Perczel *et al.*, Topological quantum optics in two-dimensional atomic arrays. *Phys. Rev. Lett.* **119**, 023603 (2017).
36. J. Perczel *et al.*, Photonic band structure of two-dimensional atomic lattices. *Phys. Rev. A* **96**, 063801 (2017).
37. I. Bloch, J. Dalibard, S. Nascimbene, Quantum simulations with ultracold quantum gases. *Nat. Phys.* **8**, 267–276 (2012).
38. J. A. Muniz, "Nanoscopic atomic lattices with light-mediated interactions," PhD thesis, California Institute of Technology, Pasadena, CA (2017).
39. S.-P. Yu, "Nano-photonic platform for atom-light interaction," PhD thesis, California Institute of Technology, Pasadena, CA (2017).
40. S.-P. Yu *et al.*, Nanowire photonic crystal waveguides for single-atom trapping and strong light-matter interactions. *Appl. Phys. Lett.* **104**, 111103 (2014).
41. H. Kosaka *et al.*, Self-collimating phenomena in photonic crystals. *Appl. Phys. Lett.* **74**, 1212–1214 (1999).
42. R. Iliew *et al.*, Diffractionless propagation of light in a low-index photonic-crystal film. *Appl. Phys. Lett.* **85**, 5854–5856 (2004).
43. G. S. Agarwal, Quantum electrodynamics in the presence of dielectrics and conductors. IV. General theory for spontaneous emission in finite geometries. *Phys. Rev. A* **12**, 1475–1497 (1975).
44. L. Novotny, B. Hecht, *Principles of Nano-Optics* (Cambridge University Press, 2012).
45. C.-L. Hung, S. M. Meenehan, D. E. Chang, O. Painter, H. J. Kimble, Trapped atoms in one-dimensional photonic crystals. *New J. Phys.* **15**, 083026 (2013).
46. D. A. Steck, Cesium D line data. Version 1.6. http://steck.us/alkalidata/. Accessed 31 May 2019.
47. K. Roy-Choudhury, S. Hughes, Quantum theory of the emission spectrum from quantum dots coupled to structured photonic reservoirs and acoustic phonons. *Phys. Rev. B* **92**, 205406 (2015).
48. A. González-Tudela, J. I. Cirac, Exotic quantum dynamics and purely long-range coherent interactions in Dirac conelike baths. *Phys. Rev. A* **97**, 043831 (2018).
49. J. Witzens, M. Loncar, A. Scherer, Self-collimation in planar photonic crystals. *IEEE J. Selected Top. Quantum Electron.* **8**, 1246–1257 (2002).
50. A. Mekis, M. Meier, A. Dodabalapur, R. E. Slusher, J. D. Joannopoulos, Lasing mechanism in two-dimensional photonic crystal lasers. *Appl. Phys. A* **69**, 111–114 (1999).
51. F. Galve, A. Mandarino, M. Paris, C. Benedetti, R. Zambrini, Microscopic description for the emergence of collective dissipation in extended quantum systems. *Sci. Rep.* **7**, 42050 (2017).
52. S. John, J. Wang, Quantum electrodynamics near a photonic band gap: Photon bound states and dressed atoms. *Phys. Rev. Lett.* **64**, 2418–2421 (1990).
53. G. Kurizki, Two-atom resonant radiative coupling in photonic band structures. *Phys. Rev. A* **42**, 2915–2924 (1990).
54. R. L. Lynge Eriksen, V. R. Daria, J. Gluckstad, Fully dynamic multiple-beam optical tweezers. *Opt. Express.* **10**, 597–602 (2002).
55. F. Wen, S. David, X. Checoury, M. El Kurdi, P. Boucaud, Two-dimensional photonic crystals with large complete photonic band gaps in both TE and TM polarizations. *Opt. Express.* **16**, 12278–12289 (2008).
56. P. Lodahl *et al.*, Chiral quantum optics. *Nature* **541**, 473–480 (2017).
57. D. Schrader *et al.*, An optical conveyor belt for single neutral atoms. *Appl. Phys. B* **73**, 819–824 (2001).
58. S. Y. Buhmann, D.-G. Welsch, Dispersion forces in macroscopic quantum electrodynamics. *Prog. Quantum Electron.* **31**, 51–130 (2007).
59. B. J. Lester, N. Luick, A. M. Kaufman, C. M. Reynolds, C. A. Regal, Rapid production of uniformly filled arrays of neutral atoms. *Phys. Rev. Lett.* **115**, 073003 (2015).
60. M. Endres *et al.*, Atom-by-atom assembly of defect-free one-dimensional cold atom arrays. *Science* **354**, 1024–1027 (2016).
61. D. Barredo, S. de Léséleuc, V. Lienhard, T. Lahaye, A. Browaeys, An atom-by-atom assembler of defect-free arbitrary two-dimensional atomic arrays. *Science* **354**, 1021–1023 (2016).
62. N. P. Stern, D. J. Alton, H. J. Kimble, Simulations of atomic trajectories near a dielectric surface. *New J. Phys.* **13**, 085004 (2011).
63. R. Ritter *et al.*, Coupling thermal atomic vapor to slot waveguides. *Phys. Rev. X* **8**, 021032 (2018).
64. A. D. Cronin, J. Schmiedmayer, D. E. Pritchard, Optics and interferometry with atoms and molecules. *Rev. Mod. Phys.* **81**, 1051–1129 (2009).

65. M. Oria, M. Chevrollier, D. Bloch, M. Fichet, M. Ducloy, Spectral observation of surface-induced van der Waals attraction on atomic vapour. *Europhys. Lett.* **14**, 527–532 (1991).
66. M. Chevrollier, D. Bloch, G. Rahmat, M. Ducloy, Van der Waals-induced spectral distortions in selective-reflection spectroscopy of Cs vapor: The strong atom–surface interaction regime. *Opt. Lett.* **16**, 1879–1881 (1991).
67. D. Bloch, M. Ducloy, "Atom-wall interaction" in *Advances in Atomic, Molecular, and Optical Physics*, E. Arimondo, H. Perrin, S. Yelin, Eds. (Academic Press, 2005), vol. 50, pp. 91–154.
68. J. D. Cohen, S. M. Meenehan, O. Painter, Optical coupling to nanoscale optomechanical cavities for near quantum-limited motion transduction. *Opt. Express.* **21**, 11227–11236 (2013).
69. S.-G. Lee, J.-S. Choi, J.-E. Kim, H. Yong Park, C.-S. Kee, Reflection minimization at two-dimensional photonic crystal interfaces. *Opt. Express.* **16**, 4270–4277 (2008).
70. Y. Tanaka *et al.*, Group velocity dependence of propagation losses in single-line-defect photonic crystal waveguides on GaAs membranes. *Electron. Lett.* **40**, 174–176 (2004).
71. COMSOL AB, Stockholm, Sweden, Comsol multiphysics. http://www.comsol.com. Accessed 31 May 2019.
72. A. F. Oskooi *et al.*, A flexible free-software package for electromagnetic simulations by the FDTD method. *Comput. Phys. Commun.* **181**, 687–702 (2010).
73. Lumerical Inc., 3D/2D Maxwell's solver for nanophotonic devices. http://www.lumerical.com/tcad-products/fdtd/. Accessed 31 May 2019.